Title:

Multivariate Spectral Analysis of pH SERS Probes for Improved Sensing Capabilities

Author names and affiliation:

Adam Williams[a], Kevin John Flynn[b], Zhidao Xia[c]& Peter Roger Dunstan[a,†]

[a]Department of Physics and Centre for Nanohealth, College of Science, Swansea University, Singleton Park, Swansea, SA2 8PP, UK

[b]Centre for Sustainable Aquatic Research, Swansea University, Singleton Park, Swansea, SA2 8PP, UK

[c]College of Medicine and Centre for Nanohealth, Swansea University, Singleton Park, Swansea, SA2 8PP, UK

Corresponding author: [†]

Peter Roger Dunstan

Department of Physics, College of Science, Swansea University, Singleton Park, Swansea, SA2 8PP, UK

P.R.Dunstan@swansea.ac.uk

Present address:

Department of Physics, College of Science, Swansea University, Singleton Park, Swansea, SA2 8PP, UK

Abstract

Adsorption of functional groups to the surface of plasmonic nanoparticles provides a platform for localised optical sensing. Over the past decade nanoscale sensors for intracellular pH measurement based on surface enhanced Raman spectroscopy (SERS) have been developed. However, the approaches by which pH-SERS measurements are made and analysed can greatly impact the precision and accuracy of pH calibration. To improve pH nanosensors the sources of experimental variation must be determined and the data optimally analysed. Here we report the plasmon-induced decarboxylation of para-mercaptobenzoic acid (pMBA) pH-reporters attached to gold nanoparticles, and conclude a strong association to laser power. The detrimental decarboxylation of pMBA has profound implications for the sensitivity and reliability of the pH sensor. Decarboxylation spectral signatures map directly onto those that are typically used to record pH changes and hence the greatest implication of decarboxylation of pH sensors is inaccurate or false pH reporting. Here a more robust spectral analysis for pH sensing based upon an optimal spectral region for pH calibration is presented together with a unique application of the multivariate statistical technique, principal components analysis (PCA). PCA interprets complex spectral dynamics and by direct comparisons with the typically employed ratio-metric analysis a significant improvement in generating accurate pH sensing is demonstrated. An application of these methods in determining the pH of internalised nanosensors in macrophage cells further promotes these step-changes in pH measurement methodology via the avoidance of disruptive spectral signatures that arise in real applications.

Introduction

Noble metal nanoparticles have been widely exploited in the field of Raman spectroscopy to act as enhancing agents which boost Raman signals through electromagnetic & chemical enhancement mechanisms [1, 2]. This technique is usually referred as surface enhanced Raman spectroscopy (SERS). The vast increase in Raman scattering events observed though surface enhancement provides a platform for the detection of native biological components from within complex biological matrices [3], and even the detection of single molecules [4, 5].

Gold (Au) and silver (Ag) nanoparticles are common place in SERS experiments as their optical properties are tuneable by particle size, thus offering the potential of the plasmon resonance frequency to be matched to the laser excitation wavelength [6–8]. The localised surface enhancement is electromagnetic and evanescent in nature, decaying exponentially away from the surface of the nanoparticle, hence molecules that occupy the nano-vicinity of the nanoparticle will experience the greatest Raman enhancements. This property is one that lends itself to the promotion of linking functionalised nanoparticle reporters, whose spectral response will be enhanced by the presence of the nanoparticle. The linked reporter can have functional groups that have a specific role, such as monitoring pH [9–11], glucose concentrations [12, 13] and intracellular redox potentials [14].

A variety of molecules have been presented which pose pH sensing capabilities through the monitoring and calibration of conformational changes presented in their Raman spectra, these molecules include; para-Mercaptobezoic acid (pMBA) [9, 10, 15,16], 2-aminothiophenol (2-ABT) [17], 4-aminothiophenol (4-ABT)[18,19], 2,5-dimercaptobenzoic acid (2,5-DMBA) [20], 3,5-

dimercaptobenzoic acid (3,5-DMBA)[21] and 4-mercaptopyridine (4-MPy)[22] . The method typically employed in calibrating the optical response of the functional group involves the ratio-metric analysis of two strong Raman modes and characterising how these peak ratios evolve as a function of pH.

In biological systems the monitoring of intracellular pH is fundamental to gain a greater understanding into biochemical mechanisms. For example, pH has a great influence over protein conformation [23], enzyme optimisation [24] and the capability of measuring intracellular pH permit studies of physiological processes, such as monitoring pH changes during endocytosis [25].

Whilst pH presents itself as an important factor to monitor it is also one that requires both true and precise measurements. The precision of any measurement is determined by the reproducibility which requires all sources of experimental variability to be minimised, whilst the trueness of a predictive result is ultimately determined by a model fitting of the calibration data. The difficulty observed in current pH sensing literature using nanoparticles and Raman spectroscopy is related to precision. The precision is typically derived from the standard deviation of the peak ratio values; if error bars are large and overlap with neighbouring calibration data points, then it is difficult to distinguish between them and thus hinder the precision of intracellular measurement.

Developments in the field have been made experimentally, for example utilising hollow Au nanoparticles has additional benefits of increasing the plasmonic response of the pH sensor[15]. This has enabled improvements in reproducibility because the strong SERS response will allow single nanoparticles to sense, whilst aggregates are required for solid nanoparticles[9];. However, uncontrollable nanoparticle aggregation will occur when aqueous ionic species screen the stabilising surface terminations.Aggregation induces large spectral variability because of a variation in the electric double layer (EDL) at the nanoparticle's surface[9]. The EDL has a geometric dependence and varies because nanoparticle aggregates form non-uniformly; the inconsistent EDL induces variations in the hydrogen ion concentration in the near vicinity of the nanoparticle (Debye thickness) resulting in fluctuating local pH values.

When introduced the biological environments, either culture media or intracellular fluid, ionic species will be present thus cause nanoparticle aggregation. It would be anticipated that this would occur to nanoparticle systems which have shown improvements in spectral reproducibility in *ex-situ* measurements. In this work efforts are concentrated on optimally analysing the spectral data to improve pH sensitivity. In doing this, the described analysis can be translated to other pH sensing platforms which have improved experimental reproducibility, with the hope of further enhancing pH sensitivity.

In this study pMBA is employed as a pH reporter adsorbed to the surface of 30nm Au nanoparticles and investigated with the aim to improve the precision of the pH nanoprobe and decrease the number of overlapping calibration points. We report on the plasmon induced decarboxylation of pMBA and its affects on the reproducibility of Raman measurements, as

decarboxylation generates spectral dynamics which map directly to a change of pH. Additionally we report on the use of principal components analysis (PCA) to derive quantitative information about subtle spectral changes induced by pH. Finally, we consider a more reliable and appropriate spectral region to monitor pH changes when using pMBA. Overall, consideration is given to these factors and how they improve the discrimination between calibration data sets and minimise false reporting of pH. The application of the pH reporter nanoparticles to a macrophage cell is examined and an *in-situ* probe measurement analysed to report the intracellular pH.

Method and Preparation

pMBA Nanoparticle Preparation

A 3mM solution of para-Mercaptobenzoic acid (Sigma-Aldrich) was prepared in ethanol (Fisher-Scientific). 10μL of 3mMpMBA solution was then added to 100μL of 30nm Au nanoparticles in aqueous solution (Nanocs, citrate terminated) and vortexed for one minute in 1.5mL Eppendorf Safe-Lock microcentrifuge tubes where the pMBA self assembled monolayer (SAM) is left to form for 90 minutes at room temperature. A 3mM solution was used for all functionalisations to ensure concentration dependent spectral changes, observed by Michota and Bukowska[26], are not encountered. Moreover at this concentration full surface coverage is reported[9].

Calibration Measurements

Samples associated with the calibration data series were produced by dropcasting 10μL of functionalised nanoparticles onto cleaned glass coverslips and allowed to dry under ambient conditions as shown in Fig. 1(a). Once dry, coverslips were flooded with buffer pH solutions to remove residual pMBA solution and any nanoparticles that had not adhered to the coverslip, Fig. 1(b). To conduct SERS measurements, aluminium liquid wells were constructed by combining a dimpled aluminium substrate and filling with pH calibration buffer solution, Fig. 1(c). The final stage is capping the pH buffer with a functionalised nanoparticle coverslip as shown in Fig. 1(d). Performing measurements in this manner as opposed to flooding the coverslips with buffer solution prevents issues associated with focusing through a convex liquid droplet (which is prone to evaporation and therefore can cause focus drift). Functionalised coverslips are not reused once the data for a particular pH has been completed.

Using an upright microscope system (Leica Microsystems) and an inVia Raman spectrometer (Renishaw ltd) equipped with a 785nm diode laser, a 50X (N/A = 0.75) microscope objective (Leica) is used to locate the drying edge of the dropcast nanoparticles where the strongest optical response of the pMBA was established. Once located the laser spot was focused through the glass coverslip and onto the nanoparticles, which reside on the lower face immersed within the buffer solution. Raman measurement parameters include a total acquisition time of 60 seconds (1s exposure accumulated 60 times) at 1.7mW (10% laser power, pin hole inserted) and centred at 1240 cm^{-1} the calibration data set typically consists of 25 Raman measurements from different locations within each sample. Although high signal to noise is required for calibration measurements, 1s exposures accumulated 60 times, as opposed to a single 60s exposure, were used so that a real time monitoring of the nanoparticle response and decarboxylation can be observed, despite the increase in shot noise. If decarboxylation is detected then the

measurement position is altered. Note, the decarboxylation of pMBA is a phenomena discussed in this paper.

The spectrometer was calibrated using a set of neon lines and wavelength reproducibility checked using an internal silicon reference sample (520 cm^{-1}) on an experiment by experiment basis. Initial calibration measurements were conducted in standard buffer solutions (Oakton) at pH values: 1.68, 4.01, 7,9.18, 10.01 and augmented with additional pH values: 4.37, 5.08, 5.67, 5.86 by mixing relative quantities of 0.1M potassium hydrogen phthalate and 0.1M NaOH. The pH of these buffer solutions was verified using a bench top pH meter (Mettler Toledo FiveEasy).

Macrophage Measurements

Murine macrophage cell line, RAW 264.7 used in this study were cultivated using Dulbecco's Modified Eagle Medium (DMEM, Life Technologies, Paisley, UK) made of 10% Fetal Bovine Serum (FBS, Biosera) and 1% antibiotics (penicillin/streptomycin, Life Technologies, Paisley, UK), in 10 cm petri dishes (GrienerBioOne, Gloucestershire, UK) and maintained at 37°C, 95% air and 5% CO_2. Cells were scraped from the petri dishes for the study and seeded at 1 $\times 10^4$ cells/cm^2, onto sterilised glass coverslips and grown at 37°C for 72 hours. At this stage the majority of the culture medium was removed, 50μL of as prepared pMBA-nanoparticles were added to the macrophage-coverslip and after a 6 hour incubation period, 200μL of growth media was reintroduced to the macrophage-nanoparticle sample where it was incubated for a further 20 hours. The lysosome pH investigation required the macrophage-nanoparticle samples to be washed thoroughly in PBS to remove any free nanoparticles and residual growth media, an aluminium well was then filled with PBS and the macrophage-nanoparticle coverslip used to cap the well.

To locate lysosomes containing pH nanoprobes, low power (1mW) 1s acquisition Raman mapping measurements were conducted with low spatial resolution. Due to the quick and rapid techniques employed, the Raman maps were very rudimentary. However they were suitable to produce low signal to noise spectra which were used to locate regions within organisms where benzene ring breathing modes were found. Higher signal-to-noise measurements (1s exposure accumulated 210 times) were then collected at these locations.

Data processing and Analysis

Spectral processing is required to truly compare the calibration data set and evaluate which spectral regions are pH sensitive. This information was subsequently used to predict a pH value based on the SERS response of internalised pMBA probes within macrophage lysosomes. Spectra produced by Window-based Raman Environment (WiRE 3.2, Renishaw) are exported as .txt files and imported into a semi-automated spectral analysis tool designed (in-house) in Wolfram Mathematica. Spectra were baseline subtracted utilising a rolling circle filter (RCF) adapted from James et al.[27] and normalised to the ν_{12} mode (1078 cm^{-1}). Spectra are segmented to the spectral region (780 – 895cm^{-1}) which has been deemed most sensitive to pH and finally analysed using PCA. PCA requires the computation of a covariance matrix and the evaluation of the associated eigenvalues & eigenvectors which are extracted using a singular value

decomposition (SVD). Finally, to form a calibration curve, PC scores are extracted and fitted with a Boltzmann sigmoidal function to allow pH values to be predicted from within macrophage lysosomes.

Results

pH sensitive Raman spectra

Samples of pMBA-nanoparticle were prepared, immersed in calibration buffer solutions and irradiated by 785 nm laser light. The spectra were found to be highly reproducible, 25 individual spectra were collected from different locations on each sample and were collated to form the calibration data, the mean of each pH group is presented in Fig. 2. To ensure that nanoparticle functionalisation has occurred checks are made on the sulfhydryl (SH) Raman mode at 2580 cm^{-1}. This mode is seen in the Raman spectrum of pure pMBA but is not observed in the SERS spectrum of functionalised nanoparticles (extended spectrum not shown here). This has been previously reported as a key indicator that pMBA is adsorbed to the nanoparticle surface [26] and that the functionalisation process is successful.

The SERS spectrum of pMBA is highly sensitive to pH thus when discussing the dynamics of pH sensitive modes it is convenient to have a global point of reference. Hence, the spectra presented in Fig. 2 have been normalised to the most prominent Raman feature which appears to have no pH dependence, i.e. the ν_{12} benzene ring breathing mode situated at 1078cm^{-1}. The plot is then displayed as an off-set stack. Normalisation of the data eliminates spectral fluctuations that can arise due to experimental variations as a result of laser stability, focus drift and sample uniformity between measurement locations. Whilst spectral fluctuations do not alter intrinsic peak ratios they make Raman spectral comparisons difficult. Table 1 outlines the pH sensitive modes observed in the SERS spectrum of pMBA with respect to the ν_{12} mode (Fig. 2). It is noted that the modes situated at 697, 763, 801, 1182, 1290, 1480 and 1710 cm^{-1} all decrease in intensity as the pH of the buffer solution increases, whereas the Raman bands at 722, 778, 849, 857, 1015, 1140, 1395 - 1424 cm^{-1} increase in intensity as the buffer pH increases. Detailed examination of the data set shown in Fig. 2 also indicates that the peak maxima at 857$cm^{-1}$and 1591cm^{-1} become red shifted to 849cm^{-1} and 1588cm^{-1} respectively with increasing pH, conversely the spectra also indicate that the maxima at 1395cm^{-1}shifts to 1424cm^{-1} as pH increases. The shift of ν_{8a}(Fig. 2 inset) ring stretching mode has been suggested to be due to the coupling between the ring stretching mode and the carboxylic group stretching mode[28].

Decarboxylation of pMBA

Methods for calibrating the optical response of functionalised nanoparticles is limited in literature, where taking a particular ratio between selected peak intensities is the most frequently utilised method. Typically the strongest Raman peaks associated with the ν_{12} (1078cm^{-1}) and ν_{8a} (1591cm^{-1}) benzene ring modes are used to reference a single pH sensitive peak; usually a vibrational mode of the carboxylic group, either the COO^- mode at 1424 cm^{-1} or the C=O (which indicates the presence of neutral carboxylic acid groups [26]) at 1710cm^{-1}. One of the motivations for this study was to produce an accurate calibration curve where the sources of experimental variations were identified and minimised.

Fig. 3 presents the evolution of the SERS spectrum of pMBA-nanoprobes (in a pH buffer of 9.18) over sequential acquisitions of twenty seconds, using a laser power of 17 mW. The data has been normalised to the ν_{12} (1078cm^{-1}) mode and its noted that the Raman modes at 1591, 1424, 1140 and 849 cm^{-1} all decrease in intensity with respect to the ν_{12} mode over consecutive acquisitions. It can also be seen that the 998, 1022 and 1575 cm^{-1} modes all increase in intensity with respect to ν_{12}. Michota and Bukowska outline these peaks and attribute them to be characteristic of monosubstituted benzene derivatives and the wavenumber/relative intensities correspond well to the SERS spectrum of thiophenol adsorbed onto Ag and Au electrodes, thus supporting the conclusion that pMBA undergoes decarboxylation during the adsorption to the electrodes whose roughness aids the decarboxylation process [26].

Based on Fig. 3 and the conclusions of Michota and Bukowska, we propose that the use of high laser powers (17mW), combined with the functionalization to gold nanoparticles, causes the decarboxylation of the adsorbed pMBA molecules. This effect was studied at various laser powers and it can be greatly diminished by decreasing the laser power to ~2 mW. This can also be demonstrated by comparing the pH 9.18 spectrum in Fig. 3 (after 60 seconds) and the identical pH in Fig. 2. Further investigations outline higher pH solutions are more likely to induce decarboxylation (e.g. pH 10.01 the decarboxylation occurs at powers above 2 mW) whilst decarboxylation is not observed at lower pH values (e.g. pH 1.68) for the range of powers tested (0.17mW – 17 mW). It was also noted that pure pMBA dropcast onto cleaned glass coverslip did not express spectral signatures of decarboxylation when the laser power was increased to ~200 mW thus determining that the decarboxylation is promoted by the gold nanoparticle and is plasmonic in origin. These results compliment the findings of Zong et al.[29] It should be noted that this decarboxylation threshold is system specific and thus dependent on the nanoparticle (silver, gold, solid, hollow), the wavelength and the power.

Whilst observation of the COO^- (1424 cm^{-1}) Raman mode has significant relevance to pH sensing, inducing decarboxylation decreases the number of carboxyl terminals and hence the intensity of COO^- relative to ν_{12} decreases. Note that ν_{12} is also the prominent Raman mode of thiophenol[30]. As discussed, the COO^- mode is often documented in the literature [9,11,15,16] to be exclusively used in spectral ratios to determine and calibrate the pH optical response of pMBA-nanoprobes. However, it can be seen in Fig. 3 that plasmon-induced decarboxylation represents a significant possibility when conducting Raman measurements. This has three main implications for calibration and pH prediction. Firstly decarboxylation will lead to detrimental issues as the resulting error bars are likely to be large since the intensity of the pH sensitive modes become modified by decarboxylation. Secondly, the spectral feature dynamics associated with decarboxylation are precisely the same as those which would detect a lowering of the solution pH. Thirdly, sequential measurements are relevant for experiments that aim to monitor pH changes over time, thus these types of experiments must ensure that the pH reporters are not susceptible to photo-induced modification. From the comparison studies we have conducted it is important to highlight that there is spectral evidence of unattributed decarboxylation found within the pH SERS literature.

Calibration: Ratio-Metric Method

The work presented in this paper aims to outline that the sensitivity of pH nanoprobes can be improved based on the employed analysis technique and thus an improvement which is transferable to other groups, including those using alternative molecules and plasmonic platforms.

However, the principal components analysis (PCA) method described later cannot be compared against the ratiometric based calibration graphs presented within the literature without considering other factors and hence the paper also conducts ratiometric analysis found in the literature. Note, no spectral processing occurs at this stage. Fig. 4 presents the resultant calibration curves from the ratio-metric analysis of $I_{COO^-}/I\nu_{8a}$ [9, 15] (red) and $I_{COO^-}/I\nu_{12}$ [11] (black).

From the perspective of making pH predictions based on the formulated calibration graphs, it is important that the resulting analysis outputs are able to distinguish between pH datasets i.e. the overlap between neighbouring error bars is minimal and can be a qualitative assessment of the analysis technique.

From Fig. 4 separations between datasets can be seen at pH 1.68 and 4.01, pH 4.01 and 6.86, pH 6.86 and 7, pH 7 and 9.18 for both $I_{COO^-}/I\nu_{8a}$ and $I_{COO^-}/I\nu_{12}$. Fig.4 also outlines ~50% overlap between pH 9.18 and 10.01 for $I_{COO^-}/I\nu_{12}$, whilst the error bars of pH 4.01 fully encompass the values of pH 4.37, 5.08, 5.67 and 5.86. On this basis it would not be possible to accurately determine the pH of any measurement within this range, severely limiting the application of the pH reporters in the biologically important pH range of 4-7.5.

Overall, when these calibration graphs are compared with the respective literature which display error bars[9, 15], Fig. 4 has smaller error bars which was concluded to be a direct result of careful consideration of experimental parameters which prevent decarboxylation whilst maintaining Raman spectra with good signal-to-noise.

Please note that the y-axis of Fig. 4 has been normalised and scaled in order to facilitate the direct comparisons between the overlap and separation of the error bars across the different analysis methodologies.

Calibration: PCA Method

Principal components analysis (PCA) is a mathematical technique typically used in multivariate data analysis. The purpose of using PCA is to utilise a greater amount of spectral information so as to increase the sensitivity of the pH sensor. The ratio-metric approach is limited to using only two pieces of information (the intensity of two Raman modes). In the terminology of PCA these pieces of information are called variables; hence the ratio-metric approach is a bi-variate analysis. In the proceeding section a segmented spectral region involving 101 wavenumbers is used, therefore this analysis has 101 variables.

PCA aims to take a series of data composed of many variables and reduce its dimensionality; this is achieved by modifying the original data so that the important information is contained

within a reduced number of variables. Important information is considered as those variables which have large variance and hence are ones which make one dataset different from another. The modification to the original data is achieved by applying high dimensional rotations, mathematically denoted as a change of basis.

PCA allows the interpretation of many spectral features simultaneously, evaluating spectral differences which relate to intensity variations of many peaks relative to each other, peak shapes and peak shifts. By taking into account much more quantitative information about the pH dynamics, PCA is applied with the aim of decreasing the number of overlapping calibration data points and their subsequent standard deviation to ultimately improve the accuracy of the pH evaluation.
A secondary benefit of the analysis are the spectral loadings, these are the high dimensional rotations which are responsible for maximised variance in the dataset. The spectral loadings are an important tool used to visualise spectral changes within the dataset offering an insight into the spectral dynamics of the data. The PC loadings are used to compute the modified data points denoted as PC scores.

Fig. 5 outlines the segmented spectral region 780 - 895cm^{-1} of the calibration dataset which was analysed by PCA. This region was chosen because it allows good discrimination between the Raman spectra obtained in different buffer solutions. One advantage of selecting this spectral region is associated with avoiding the background fluorescent nature of the underlying glass substrate, the importance of which will be demonstrated on the macrophage measurements.

A typical output of PCA is the two dimensional PC score plot, the resulting plot for the segmented data is present in Fig. 6. The PC scores associated with the first principal component (PC1) lie along the x axis and the second principal component scores (PC2) along the y axis and each point represents a single spectra. Large spatial separations between the extreme pH values are seen along PC1 and discriminations between intermediate groups along both PC1 and PC2.

The first principal component loading (PC Loading) is outlined in Fig. 7. This loading highlights what has been deemed by the PCA to be the source of maximum variance within the dataset, i.e. the PC loading visualises the spectral differences that exist within the data and so subsequently lead to the PC score separation shown in Fig. 6. The PC loading also highlights the wavenumber specific differences between the segmented calibration data.

From Fig. 7 the positive/negative behaviour of the loading indicates that the Raman mode at 801cm^{-1} in Fig. 5 exhibits the inverse relationship relative to pH than the 849cm^{-1} mode. The 801cm^{-1}mode is strong for low pH values and weak for higher pH values whereas the 849cm^{-1}mode is strongest for higher pH Values and weak of low pH values. The PC loading also highlights a shift in the maxima in the region 849 – 860cm^{-1} which is evident in Fig. 5. The features described above are complex, accounting for two qualitative features of the spectra namely peak intensity changes for two different peaks whilst simultaneously monitoring a shift in the maxima of the 849 cm^{-1} mode, these features are specifically what PCA uses to discriminate between the calibration data and offers a more comprehensive solution which bases

discrimination on features which cannot be easily accounted for using traditional ratio-metric methods.

By extracting the PC1 scores for the calibration dataset it becomes possible to formulate a calibration graph based on the principal components analysis (Fig. 8, red data). However, in order to directly compare the effect of using PCA as a method of discriminating between the pH datsets, a ratio-metric analysis of the segmented spectral region was conducted (Fig. 8, black data). Again the y-axis of Fig. 8 has been scaled in order to facilitate the direct comparisons between the overlap and separation of the error bars across the different analysis methodologies, in this case ratio-metric versus PCA.

As presented earlier, the biologically relevant pH range of 4 - 7.5 was challenging for pH discrimination particularly in the range 4.01 - 5.86 when the standard peak ratio methodology was employed, see Fig. 4. The new segmented spectral region 780 – 895cm^{-1} can exploit the peak ratio of $I_{800/}$ I_{849} and Fig .8 (black dataset) is able to distinguish an additional pH value (pH 5.86) from previously overlapping datasets. Furthermore it is observed that by selecting this new spectral region it has been possible to improve the separation between pH 1.68 and pH 4.01. This confirms that a single peak ratio does not fit all pH sensing purposes and choosing an alternative peak ratio has the potential to be more sensitive at specific pH ranges.

The calibration dataset based upon PCA in this segmented spectral region 780 - 895cm^{-1} is also shown in Fig.8 (red dataset) and illustrates the significant improvements in using the PCA routine. By comparing the error bars on the resulting calibration graph (red dataset vs black dataset) a reduction in the error bar size for 70% of the PCA data points and an overall decrease is observed in the number of overlapping groups when compared to its peak ratio counterpart. The increased discrimination of the PCA methodology is borne out by the improved reproducibility in this spectral region and the separation of pH groups.
To summarise the improvements Fig 9 presents an error bar plot to ultimately compare PCA calibrations to various ratio-metric methodologies. Fig 9 clearly outlines improvements made by the spectral region chosen (the I_{800}/I_{849} ratio) and then the application of PCA has been successful in improving the separation between the pH groups-4.01 - 4.37, thus further reducing the range over which pH datasets were inseparable in the pH group 4.01 - 5.86 (for the I_{800}/I_{849} ratio). PCA thus confines its uncertainty limitations to the pH group 4.37 - 5.67. This demonstrates a significant success for the PCA method and further promotes the reliable and robust use of the pH sensing nanoprobes to applications within biological systems.

Macrophage study

In order to promote the application of the PCA discrimination of pH sensing via an intracellular pH reporter, pMBA-nanosensors were internalised into murine macrophage cells by adding the functionalised nanosensors into the macrophage growth media (as described earlier). Macrophage lysosomes containing nanoparticles were located, as previously described. Raman measurements were conducted at these locations. Raman measurements of high signal to noise were collected over a period of 210s. Long exposure times were required because of the limited nanoparticle uptake and avoidance of increasing the laser power and creating the previously

described plasmon induced decarboxylation. Fig. 10 presents the mean Raman spectrum of 21 individual spectra from various macrophages (black) where the shaded region (grey) representing the standard deviation of the measurements.

One of the main drives for the development of pH sensitive Raman nanoprobes is to internalise them in biological samples, allowing the optical response of the probe to be interpreted and hence provide a readout of the predicted intracellular pH. Calibration curves derived from peak intensity ratios require any external contributions to the intensity of peaks to be minimised to ensure an accurate interpretation, such contributions can arise due to signal/noise, decarboxylation and/or spectral background. As seen in Fig. 3 the degree of decarboxylation affects the ratio between the established pH sensitive peaks and thus will affect the predicted pH value. Fig. 10 expresses a typical spectrum that is subject to background fluorescence associated with the interaction between the 785nm laser and the glass substrate. The fluorescent feature is broad with a maxima at ~1390 cm^{-1}, and has non-linear features along the 1100 - 1700 cm^{-1} range. This feature is prevalent within Fig.10, but is not observed in Fig. 2, because the nanoparticle number density is much less during the lysosome measurements than it is during the calibration measurements. The nanoparticle number density within the lysosomes is greatly decreased because factors, such as phagocytosis rates, can affect the number of nanoparticles within that region.

The nanoparticle number density directly affects the Raman signal and hence the fluorescence contribution is a significantly larger proportion of the total signal in this study of macrophages. Additionally the nanoparticles within each macrophage will encounter some laser power attenuation due to the cellular membrane. The wavenumber location of the background fluorescence is a significant issue because it changes the intensity value and ratios of the pH sensitive peaks, i.e. the peaks used in the literature to form the standard pH calibration curves. This in turn will clearly affect the reliability of predicting the host's intracellular pH. Furthermore the determination and removal of this background is non-trivial. For these reasons a significant advantage is gained in using the spectral region 780 - 895cm^{-1} highlighted by this study, as this region is relatively unaffected by the fluorescence background.

Predictions of the intracellular pH of the macrophage were achieved by analysed the segmented macrophage Raman spectral range 780 - 895cm^{-1} via the PCA method, and assigning PC score associated with the first principal component loading (Fig. 7). Once a PC score had been assigned to each macrophage spectrum a prediction of the pH was made from the calibration curve. The calibration curve is shown in Fig. 11 and is fitted with a Boltzmann Sigmoid function (r^2 =0.96). The 21 PC1 scores were then mapped onto the calibration and the pH range determined. The analysis conducted predicted an average lysosome pH of (5.56 ±0.33) units where the error is the standard deviation of the measurements. This value is in agreement with measured values in literature of murine macrophage cells which has a pH range of 4.5 - 7.2 throughout the endocytic cycle [31-35].

Conclusion

Following the documented development of pH sensing nanoparticles in the literature, this work has explored practical and analytical methods by which reliability and accuracy of pH

measurements can be improved when based upon the platform of pMBA functionalised gold nanoparticles used to measure intracellular pH. This required extensive consideration of a wide range of aspects that contribute to the formation of a reliable optical sensor, including the practicalities of data acquisition, spectral analysis tools, calibration methods and pH prediction methods. The study was able to systematically compare the literature based standard ratio-metrics methods with new acquisition controls, spectral regions and the development of an alternative analysis using PCA. Spectral features representing conformational changes of pMBA were tracked, based upon the sensitivity to immersion in different pH buffer solutions. However the sensitivity to laser induced plasmon decarboxylation of pMBA gives rise to significant analysis challenges and the reliability of pH prediction. We conclude that the effects of decarboxylation can be negated by the appropriate use of laser powers and that by concentrating analysis on specific spectral peaks in the region 780 - 895 cm^{-1} the issues associated with glass background fluorescence are also minimised. Moreover, analysis of spectra by PCA provided a more robust tool than ratio-metrics at identifying spectral changes that arise due to pH, and hence reduce uncertainty in pH predictions. In a comparison between calibration curves formulated by PCA and peak ratios of a selected spectral region we find that PCA provides a reduction in the uncertainty for 70% of the pH calibration data points and hence a reduction in the number of overlapping pH groups, particularly when considering the range of biological importance (pH 4 - pH 7.5). Using these new protocols, applications to intracellular pH measurements have been successfully demonstrated with macrophage cells, whereupon pH predications of 5.56 ± 0.33 were made and match well with those accepted in the literature for this system.

Acknowledgements

The authors would like to extend their thanks for the technical resources and support provided by the Centre for Nanohealth, Centre for Sustainable Aquatic Research and Department of Physics. A. Williams is also grateful to Swansea University and College of Science for financial support of his PhD studies. The authors extend their thanks to H. Intabli for her contribution to the macrophage study.

References

[1] K. A. Willets, R. P. Van Duyne. *Annu Rev Phys Chem*. **2007** ; *58* , 267.

[2] J. R. Lombardi, R. L. Birke. *Acc Chem Res*. **2009** ; *42* , 734.

[3] K. Kneipp, H. Kneipp, I. Itzkan, R. R. Dasari, M. S. Feld. *J Phys Condens Matter*. **2002** ; *14* , 597.

[4] K. Kneipp, Y. Wang, H. Kneipp, L. T. Perelman, I. Itzkan, R. R. Dasari, M. S. Feld. *Phys Rev Lett*. **1997** ; *78* , 1667.

[5] S. R. Emory, W. E. Haskins, S. Nie. *J Am Chem Soc*. **1998** ; *7863* , 8009.

[6] S. Oldenburg, R. Averitt, S. Westcott, N. Halas. *Chem Phys Lett*. **1998** ; *288* , 243.

[7] T. R. Jensen, M. D. Malinsky, C. L. Haynes, R. P. Van Duyne. *J Phys Chem B*. **2000** ; *104* , 10549.

[8] M. Hu, J. Chen, Z-Y. Li, L. Au, G. V. Hartland, X. Li, M. Marquez, Y. Xia. *Chem Soc Rev*. **2006** ; *35* , 1084.

[9] C. E. Talley, L. Jusinski, C. W. Hollars, S. M. Lane, T. Huser. *Anal Chem*. **2004** ; *76* , 7064.

[10] S. W. Bishnoi, C. J. Rozell, C. S. Levin, M. K. Gheith, B. R. Johnson, D. H. Johnson, N. J. Halas. *Nano Lett*. **2006** ; *6* , 1687.

[11] J. Kneipp, H. Kneipp, B. Wittig, K. Kneipp. *Nano Lett*. **2007** ; *7* , 2819.

[12] K. E. Shafer-Peltier, C. L. Haynes, M. R. Glucksberg, R. P. Van Duyne. *J Am Chem Soc*. **2003** ; *125* , 588.

[13] O. Lyandres, J. M. Yuen, N. C. Shah, R. P. VanDuyne, J. T. Walsh, M. R. Glucksberg. *Diabetes Technol Ther*. **2008** ; *10* , 257.

[14] C. A. R. Auchinvole, P. Richardson, C. McGuinnes, V. Mallikarjun, K. Donaldson, H. McNab, C. J. Campbell. *ACS Nano*. **2012** ; *6* , 888.

[15] A. M. Schwartzberg, T. Y. Oshiro, J. Z. Zhang, T. Huser, C. E. Talley. *Anal Chem*. **2006** ; *78* , 4732.

[16] K. Kneipp, H. Kneipp. *Beilstein J Nanotechnol*. **2013** ; *4* , 834.

[17] Z. Wang, A. Bonoiu, M. Samoc, Y. Cui, PN Prasad. *Biosens Bioelectron*. **2008** ; *23* , 886.

[18] S. Zong, Z. Wang, J. Yang, Y. Cui. *Anal Chem*. **2011** ; *83* , 4178.

[19] K. Kim, KL. Kim, D. Shin, J. Choi, KS. Shin. **2012** ; *116* , 4774.

[20] L. Lawson, T. Huser. *Anal Chem*. **2012** ; *84* , 3574.

[21] L. Lawson, J. W. Chan, T. Huser. *Nanoscale*. **2014** ; 6 , 14

[22] R. A. Jensen, J. Sherin, S. R. Emory. *Applied spectroscopy*. **2007** ; 61 , 8

[23] R. Lumry, H. Eyring. *J Phys Chem*. **1954** ; *58* , 110.

[24] A. Zaks, A. M. Klibanov. *Proc Natl Acad Sci*. **1985** ; *82* , 3192.

[25] J. Kneipp, H. Kneipp, B. Wittig, K. Kneipp. *J Phys Chem C*. **2010** ; *114* , 7421.

[26] A. Michota, J. Bukowska. *J Raman Spectrosc*. **2003** ; *34* , 21.

[27] T. M. James, M. S. Schlosser, R. J. Lewis, S. Fischer, B. Bornschein, H. H. Telle. *Appl Spectrosc*. **2013** ; *67* , 949.

[28] Y. Liu, H. Yuan, A. M. Fales, T. Vo-Dinh. *J Raman Spectrosc*. **2013** ; *44* , 980.

[29] Y. Zong, Q. Guo, M. Xu, Y. Yuan, R. Gu, J. Yao. *RSC Adv.* Royal Society of Chemistry; **2014** ; *4* , 31810.

[30] A. Tripathi, E. D. Emmons, S. D. Christesen, A. W. Fountain, J. A. Guicheteau. *J Phys Chem C.* **2013** ; *117* , 22834.

[31] K. P. Mcnamara, T. Nguyen, G. Dumitrascu, J. Ji, N. Rosenzweig, Z. Rosenzweig. **2001** ; *73* , 3240.

[32] S. Ohkuma, B. Poole. *Proc Natl Acad Sci U S A.* **1978** ; *75* , 3327.

[33] C. J. Galloway, G. E. Deant, M. Marsh, G. Rudnickt, I. . R. A. Mellman. *Proc Natl Acad Sci U S A.* **1983** ; *80* , 3334.

[34] S. A. Hilderbrand, K. A. Kelly, M. Niedre, R. Weissleder. *Bioconjug Chem.* **2008** ; *19* , 1635.

[35] Y. Fleger, M. Rosenbluh. *Res Lett Opt.* **2009** ; *2009* , 1.

Observed Peak Position (cm^{-1}) (Fig. 2)	Identified Raman Mode	Literature Peak Position (cm^{-1})	Nanoparticle Material	References
697	OCO bending, in-plane ring compression and C-S stretching	696	Au	10
722	Out of plane γ(CCC)	718	Au, Ag	24
	Out of plane ring hydrogen wagging	718	Au	10
763	-*	-	-	-
778	-*	-	-	-
801	In plane deformation, C-COOH stretching and COO^- bending	800	Au	10
849 - 857	δ(COO^-)	840	Au, Ag	24
	δ(COO^-)	845	Au, Ag	9, 28
1015	Ring deformation	1011	Au	25
1078	ν_{12}	1080	Au, Ag	24
	Ring breathing	1077	Au, Ag	9, 10, 25
	Ring breathing	1076	Au, Ag	11
	Ring breathing	1070	Au	28
1140	13-β-(CCC) + ν(C-S) + ν(C-COOH)	1140	Ag	9
	$CCOO^-$	1136.8	Au	25
	CH in plane bending	1137	Au	10
1182 - 1183	C-H in plane bending	1179.7 (low pH)	Au	25
	C-H in plane bending	1178.6 (high pH)	Au	25
1273 - 1288	-*	-	-	-
1290	δ(CH) + ν(CC)	1291	Ag	33
1395 - 1424	COO^-	1380	Ag	11, 24
	COO^-	1393	Au	10
	COO^-	1423	Au	11, 24
1480 - 1483	C-H in plane bending	1482	Au	25
1588 - 1591	ν_{8a}	1590	Au, Ag	24
	Ring Breathing	1590	Au, Ag	9, 10, 28
	Ring Breathing	1586	Au, Ag	11
	Ring Stretching	1587 (low pH)	Au	25
	Ring Stretching	1584 (high pH)	Au	25
1710	C=O stretch	1710	Au, Ag	24
	C=O stretch	1702	Au	10
	C=O stretch	1700	Au, Ag	11
	COOH stretch	1700	Au	25

* - denotes unassigned Raman modes

Table and Figure captions

Table 1: Assignment of observed Raman modes from Fig. 2 with those found in literature.

Figure 1: Schematic of the calibration sample preparations. a) functionalised nanoparticles are deposited onto cleaned glass coverslips and allowed to dry under ambient conditions, b) functionalised coverslips are flooded with buffer solution to remove residues, c) aluminium dimple platform is filled with pH buffer solution and d) functionalised coverslip caps the aluminium dimple platform.

Figure 2: The mean Raman response of pMBA functionalised nanoparticles as a function of pH. A laser power of 1.7mW was used to collect the featured Raman spectra for a total of 60s. The spectra have been linearly offset for clarity. The inset presents a pH sensitive spectral shift of the 1585cm^{-1} Raman mode.

Figure 3: pMBA-Au Nanoparticles under sequential laser acquisitions of 20 s expressing progressive decarboxylation in buffer solution pH 9.18 using a laser power of 17mW. The spectra have been normalised to the 1078cm^{-1}Raman mode and offset for clarity.

Figure 4: Calibration curves formed by analysing the calibration dataset by the standard literature peak-ratio methods, i.e. $I_{COO-}/I\nu_{8a}$ (red) and $I_{COO-}/I\nu_{12}$ (black). Note, to ensure clarity the upper x axis (red) applies only to $I_{COO-}/I\nu_{8a}$ data points (red) and has been intentionally offset from the lower x axis (black) which applies to the $I_{COO-}/I\nu_{12}$ data points (black). The data presented indicates the mean measurements and the error bars represent the standard deviation of 25 measurements.

Figure 5: Segmented spectral region analysed during the Principal Components Analysis

Figure 6: Two dimensional PC score plot for the calibration data set. Each segmented spectrum is assigned a PC score for each loading, PC scores associated with principal component 1 (PC1) lie along the x axis and principal component 2 (PC2) along the y axis

Figure 7: The first Principal Component Loading which indicates spectral differences causing separations in PC Score plots (see Fig. 6).

Figure 8: Calibration graphs by ratio method of I_{800}/ I_{849} (black points) of unprocessed data and PCA of the processed calibration data (red points). Note to ensure clarity the upper x axis (red) applies only to PC score data points (red) and has been offset from the x axis below (black) which applies to the I_{800}/ I_{849} data points (black). The data points and error bars represent the mean and standard deviation of the data.

Figure 9: An error bar plot which summarises for direct comparison the ratio-metric/PCA calibration data previously presented in Fig 4 and Fig 8 and illustrates the improvements using the PCA methodology over the ratio-metric approach.

Figure 10: Mean Raman spectrum (21) of internalised pMBA-nanoprobes in macrophage lysosomes (Black). The standard deviation of the measurements is represented by the shaded region (Grey).

Figure 11: PCA calibration curve with fitted Boltzmann sigmoidal function (r^2=0.96) used to evaluate intracellular pH values from derived macrophage PC scores.

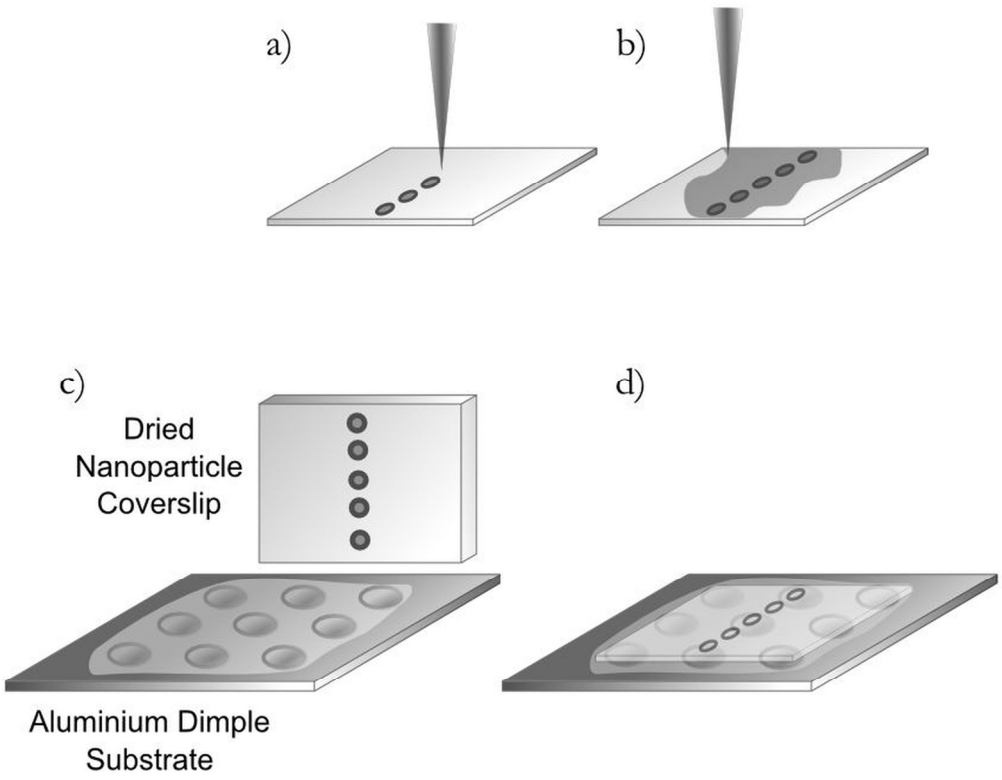

Figure 1: Schematic of the calibration sample preparations. a) functionalised nanoparticles are deposited onto cleaned glass coverslips and allowed to dry under ambient conditions, b) functionalised coverslips are flooded with buffer solution to remove residues, c) aluminium dimple platform is filled with pH buffer solution and d) functionalised coverslip caps the aluminium dimple platform.
66x53mm (600 x 600 DPI)

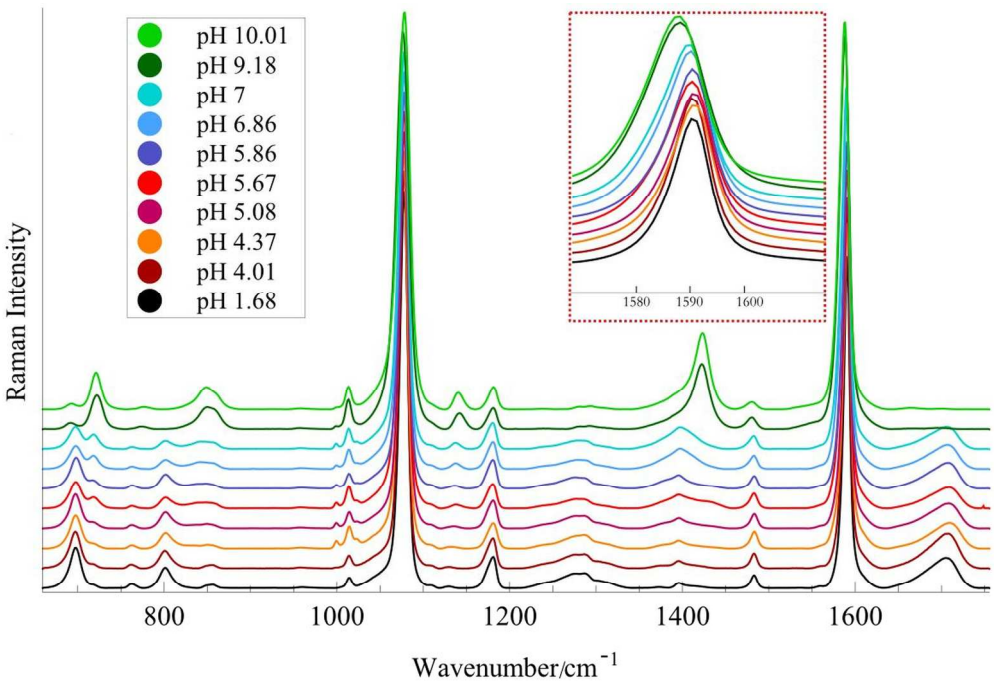

Figure 2: The mean Raman response of pMBA functionalised nanoparticles as a function of pH. A laser power of 1.7 mW was used to collect the featured Raman spectra for a total of 60 s. The spectra have been linearly offset for clarity. The inset presents a pH sensitive spectral shift of the 1585 cm^{-1} Raman mode.
114x77mm (600 x 600 DPI)

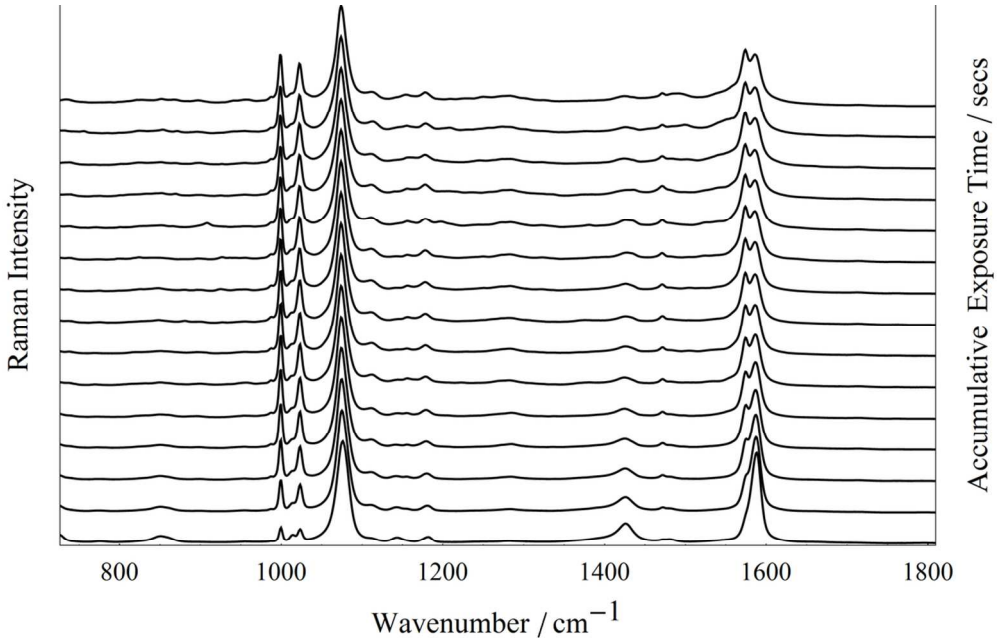

Figure 3: pMBA-Au Nanoparticles under sequential laser acquisitions of 20 s expressing progressive decarboxylation in buffer solution pH 9.18 using a laser power of 17 mW. The spectra have been normalised to the 1078 cm^{-1} Raman mode and offset for clarity.
53x34mm (600 x 600 DPI)

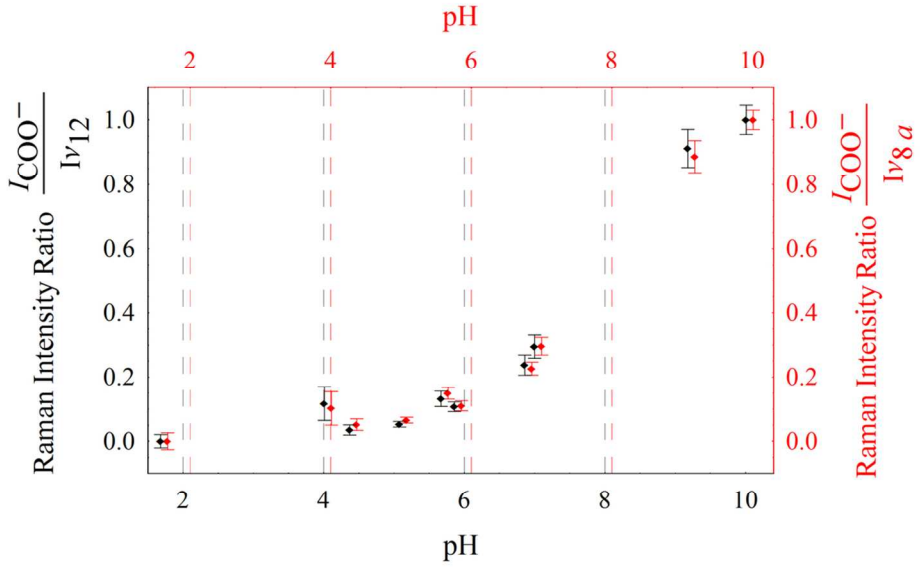

Figure 4: Calibration curves formed by analysing the calibration data set by the standard literature peak-ratio methods, i.e. I_{COO^-}/Iv_{8a} (red) and I_{COO^-}/Iv_{12} (black). Note, to ensure clarity the upper x axis (red) applies only to I_{COO^-}/Iv_{8a} data points (red) and has been intentionally offset from the lower x axis (black) which applies to the I_{COO^-}/Iv_{12} data points (black). The data presented indicates the mean measurements and the error bars represent the standard deviation of 25 measurements.
53x34mm (600 x 600 DPI)

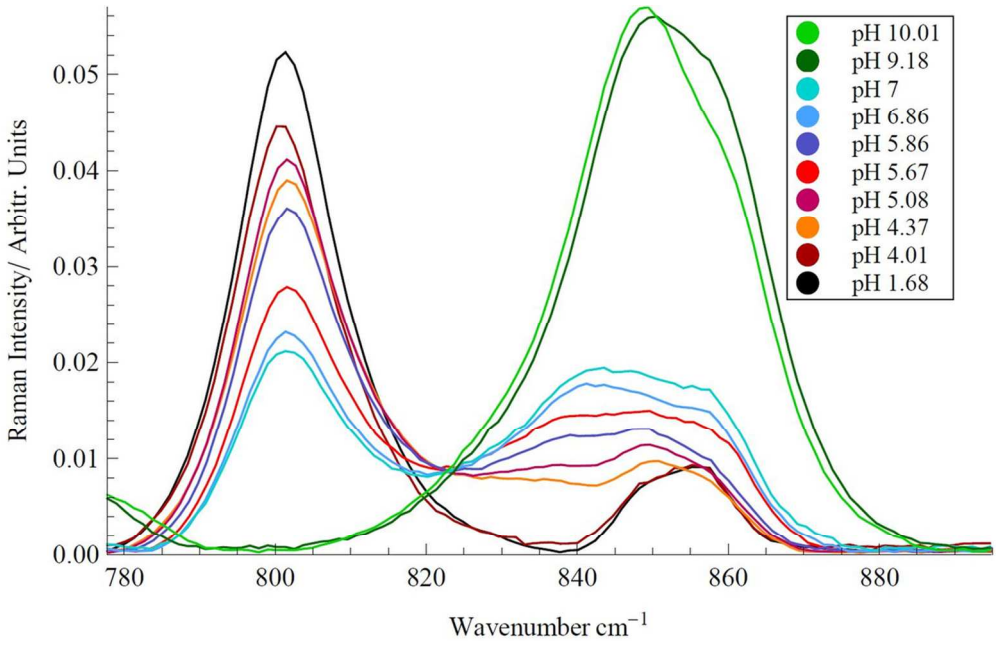

Figure 5: Segmented spectral region analysed during the Principal Components Analysis
53x34mm (600 x 600 DPI)

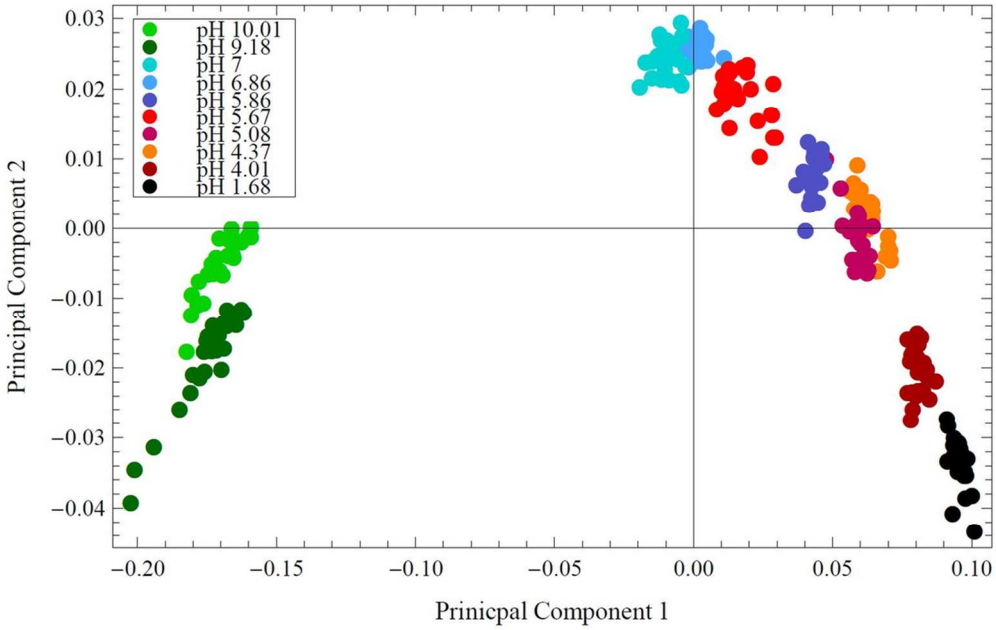

Figure 6: Two dimensional PC score plot for the calibration data set. Each segmented spectra is assigned a PC score for each loading, PC scores associated with principal component 1 (PC1) lie along the x axis and principal component 2 (PC2) along the y axis
52x33mm (600 x 600 DPI)

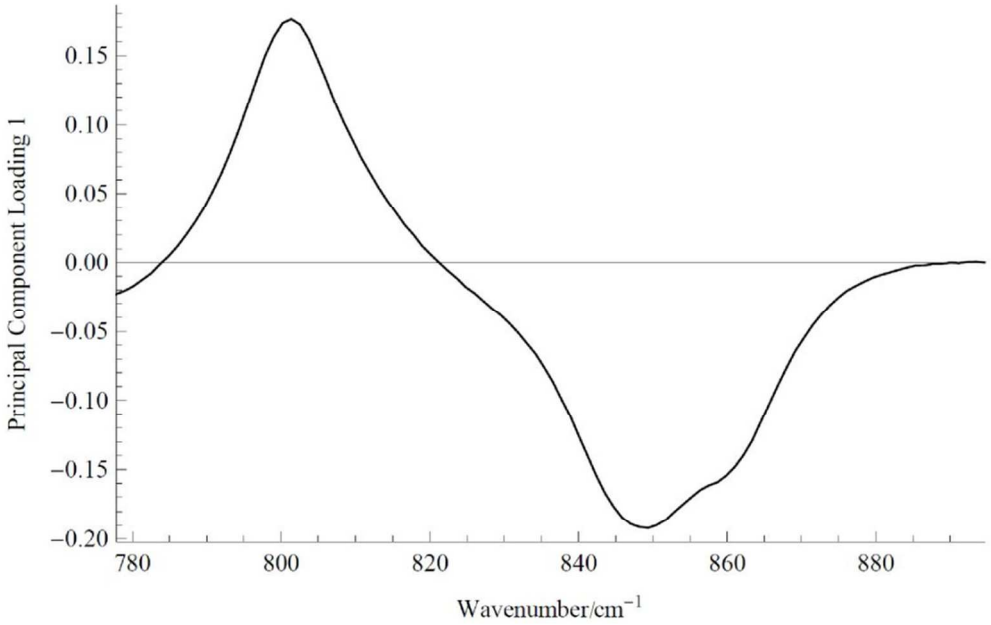

Figure 7: The first Principal Component Loading which indicates spectral differences causing separations in PC Score plots (see Fig. 6).
52x33mm (600 x 600 DPI)

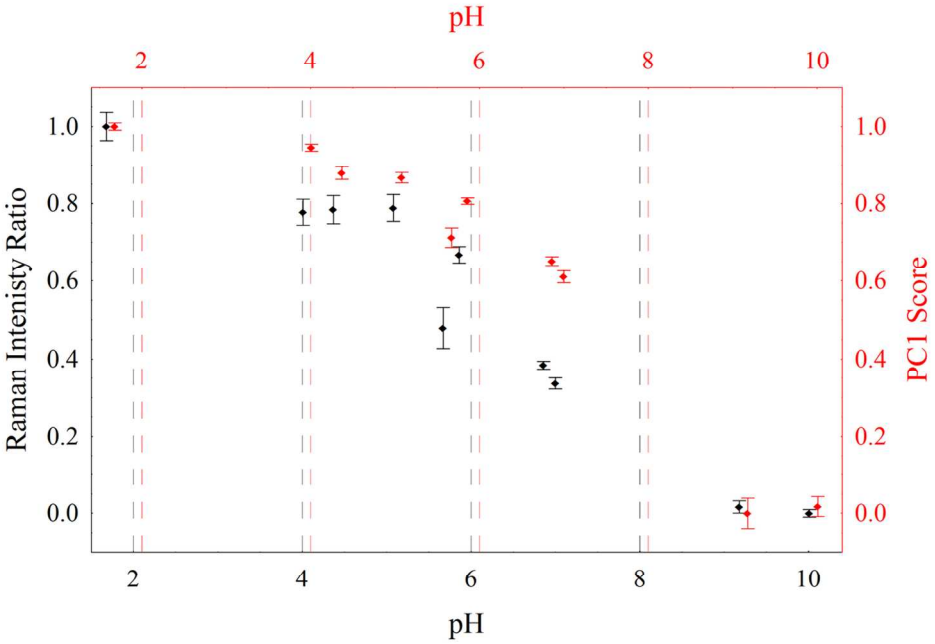

Figure 8: Calibration graphs by ratio method of I_{800} / I_{849} (black points) of unprocessed data and PCA of the processed calibration data (red points). Note to ensure clarity the upper x axis (red) applies only to PC score data points (red) and has been offset from the x axis below (black) which applies to the I_{800} / I_{849} data points (black). The data points and error bars represent the mean and standard deviation of the data.
60x43mm (600 x 600 DPI)

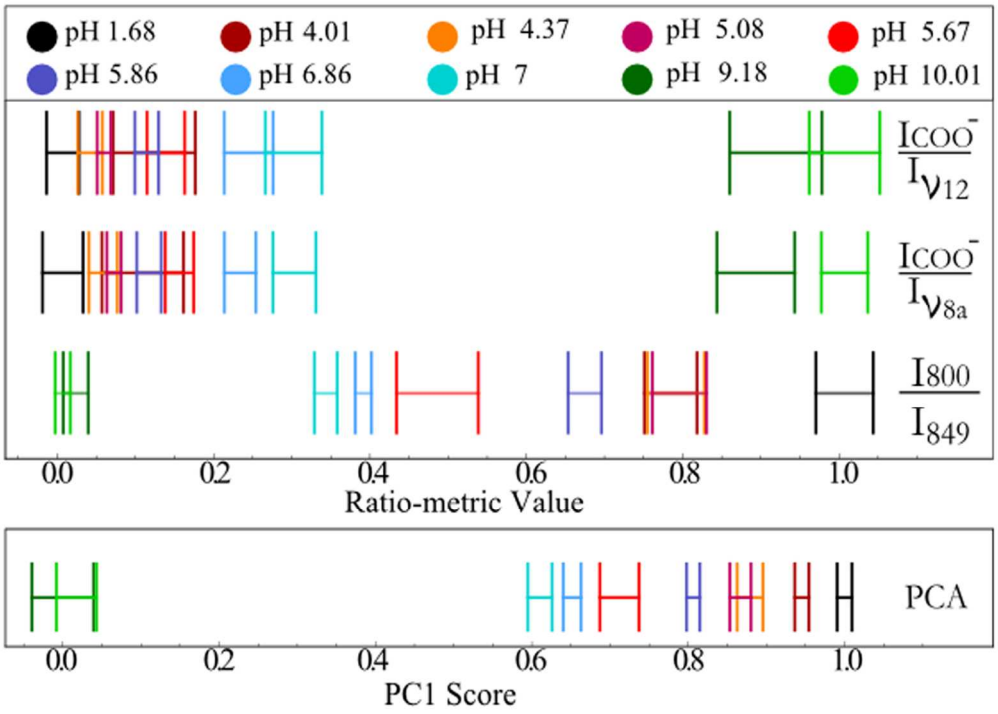

Figure 9: An error bar plot which summarises for direct comparison the ratio-metric/PCA calibration data previously presented in Fig 4 and Fig 8 and illustrates the improvements using the PCA methodology over the ratio-metric approach.
60x42mm (600 x 600 DPI)

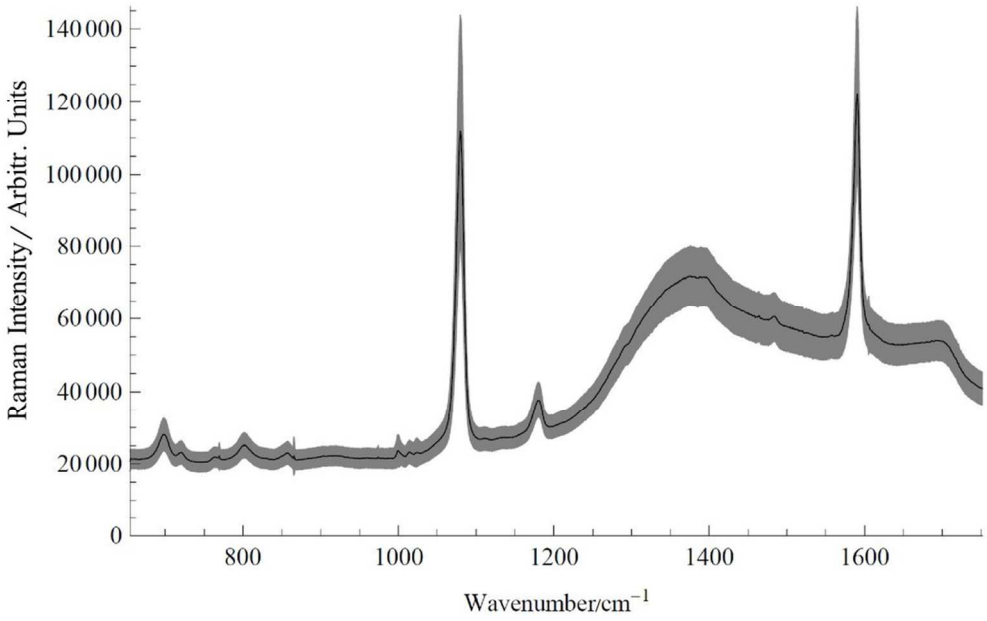

Figure 10: Mean Raman spectra (21) of internalised pMBA-nanoprobes in macrophage lysosomes (Black). The standard deviation of the measurements is represented by the shaded region (Grey).
52x32mm (600 x 600 DPI)

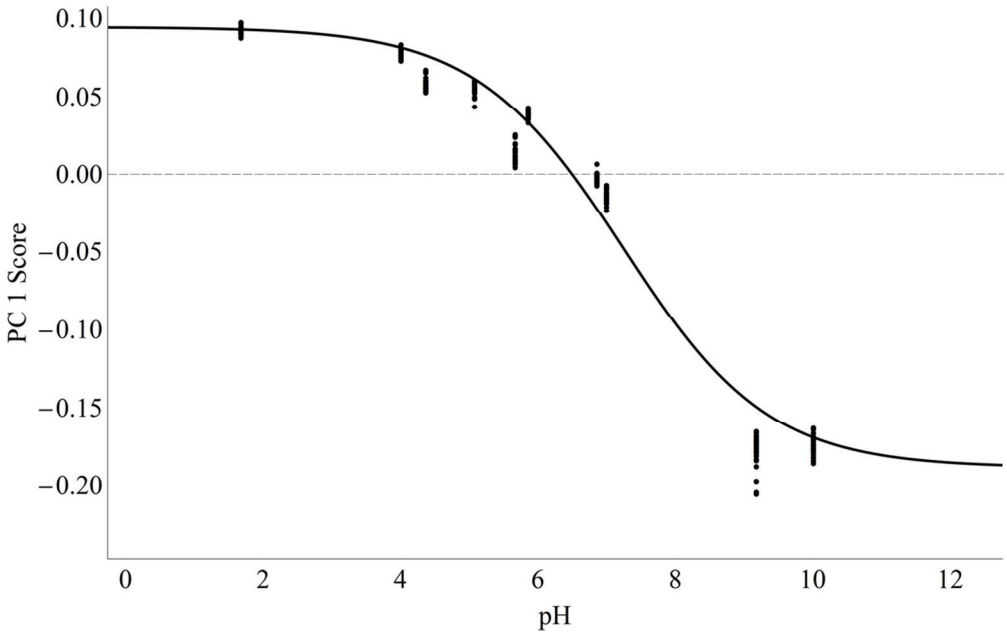

Figure 11: PCA calibration curve with fitted Boltzmann sigmoidal function (r^2=0.96) used to evaluate intracellular pH values from derived macrophage PC scores.
52x33mm (600 x 600 DPI)